Post-wildfire surface deformation near Batagay, Eastern Siberia, detected by L-band and C-band InSAR

Kazuki Yanagiya[1] and Masato Furuya[2]

[1]Department of Natural History Sciences, Graduate School of Science, Hokkaido University.

[2]Department of Earth and Planetary Dynamics, Faculty of Science, Hokkaido University.

Corresponding author: Kazuki Yanagiya (k.yanagiya@frontier.hokudai.ac.jp) and Masato Furuya (furuya@sci.hokudai.ac.jp)

Key Points:

- Post-wildfire surface deformation on the northwest of Batagay, Eastern Siberia, was detected by two independent Interferometric Synthetic Aperture Radar systems.
- L-band long-term and C-band short-term interferograms indicate the spatial and temporal complexity of the deformation in terms of both subsidence and uplift.
- Spatial heterogeneities of the subsidence magnitude were clearly correlated to the gully development, whereas the burn severity was rather homogeneous.
- Detection of enhanced uplift signals at the fire scar and its interpretation based on a physics-based frost heave theory.

Abstract

Thawing of ice-rich permafrost and subsequent ground subsidence can form characteristic landforms, and the resulting topography they create are collectively called “thermokarst”. The impact of wildfire on thermokarst development remains uncertain. Here we report on the post-wildfire ground deformation associated with the 2014 wildfire near Batagay, Eastern Siberia. We used Interferometric Synthetic Aperture Radar (InSAR) to generate both long-term (1-4 years) and short-term (sub-seasonal to seasonal) deformation maps. Based on two independent satellite-based microwave sensors, we could validate the dominance of vertical displacements and their heterogeneous distributions without relying on in-situ data. The inferred time-series based on L-band ALOS2 InSAR data indicated that the cumulative subsidence at the area of greatest magnitude was greater than 30 cm from October 2015 to June 2019, and that the rate of subsidence slowed in 2018. The burn severity was rather homogeneous, but the cumulative subsidence magnitude was larger on the east-facing slopes where the gullies were also predominantly developed. The correlation suggests that the active layer on the east-facing slopes might have been thinner before the fire. Meanwhile, C-band Sentinel-1 InSAR data with higher temporal resolution showed that the temporal evolution included episodic changes in terms of deformation rate. Moreover, we could unambiguously detect frost heave signals that were enhanced within the burned area during the early freezing season but were absent in the mid-winter. We could reasonably interpret the frost heave signals within a framework of premelting theory instead of assuming a simple freezing and subsequent volume expansion of pre-existing pore water.

Plain Language Summary

Wildfires in arctic regions not only show an immediate impact on nearby residents but also long-lasting effects on both regional ecosystems and landforms of the burned area via permafrost degradation and subsequent surface deformation. However, the observations of post-wildfire ground deformations have been limited. Using satellite-based imaging technique called Interferometric Synthetic Aperture Radar (InSAR), we detected the detailed spatial-temporal evolution of post-wildfire surface deformation in Eastern Siberia, which helps in understanding permafrost degradation processes over remote areas. Post-wildfire areas are likely to be focal points of permafrost degradation in the Arctic that can last many years.

1 Introduction

Wildfires in boreal and arctic regions are known to have increased over recent decades in terms of both frequency and areal coverage (e.g., Kasischke & Turetsky, 2006; Hu et al., 2010), and have had significant impacts on permafrost degradation (e.g., Jafarov et al., 2013; Zhang et al., 2015; Gibson et al., 2018). Although fires do not directly heat up the subsurface space deeper than 15 cm (Yoshikawa et al., 2003), severe burning decreases surface albedo, and removes vegetation and the surface organic soil layer that previously acted as insulators buffering from changes in air temperature. Subsequent increases in both soil temperature and thickness of the active layer, a near-surface layer that undergoes a seasonal freeze-thaw cycle, have been documented for up to several years after the fire (e.g., Yoshikawa et al., 2003). Meanwhile, in ice-rich permafrost regions, the thawing of permafrost and the melting of massive ice can lead to formation of characteristic landforms such as thaw pits and ponds, and retrogressive thaw slumps. While there are a variety of classifications in terms of morphological and hydrological characteristics (Jorgenson, 2013), those thaw-related landforms and the topography they create are collectively termed as “thermokarst”. However, the role of wildfires in developing thermokarst terrain remains quantitatively uncertain. Moreover, in comparison to the controlled warming experiments in Alaska (Hinkel and Hurd Jr, 2006; Wagner et al., 2018), wildfires in arctic regions may also be viewed as uncontrolled disturbance experiments that aid in understanding the permafrost degradation processes.

Ice-rich permafrost deposits, known as the yedoma ice complex (yedoma), are widely distributed in the lowland of Alaska and Eastern Siberia (Kanevskiy et al., 2011; Schirrmeister et al., 2013). The greatest subsidence within the 2007 Anaktuvuk River tundra fire scar was identified in the yedoma upland by LiDAR (Jones et al., 2015). Yedoma is a unique permafrost deposit in terms of its extraordinarily high volume of ice (50-90 %) and organic-rich sediments. While the organic carbon trapped in permafrost regions is estimated to be twice that in the current atmosphere, permafrost thawing and related thermokarst processes may release the carbon as greenhouse gasses (CO_2 and CH_4) via microbial breakdown, which may further promote global warming (Mack et al., 2011; Schuur et al., 2015). Thus, in order to estimate the volume of greenhouse gasses released, it is important to evaluate the volume of thawed ice associated with thermokarst processes in yedoma-rich areas.

Near the village of Batagay, Sakha Republic, Eastern Siberia (Figure 1), there exists the Batagaika megaslump, known as the world’s largest retrogressive thaw slump, exposing roughly 50-90 m thick yedoma deposits on the north-east facing slope (e.g., Kunitsky et al., 2013; Murton et al., 2017). Thaw slumps are characterized by a steep headwall surrounding a slump floor and develop as a result of rapid permafrost thawing. The Batagaika megaslump was initiated at the end of the 1970s by deforestation but still appears to be growing (Günther et al., 2016). Considering this feature, it is worth considering whether new disturbances in the proximity will result in the formation of similar landforms. A wildfire incident occurred in July 2014 near Batagay, which, like deforestation, will change the ground thermal regime. Therefore, it is important to examine whether future catastrophic thermokarst development could be similarly initiated at the fire scar, whose area is much larger than the Batagaika megaslump (Fig 1b).

The first objective of this study was to assess the effectiveness of satellite Interferometric Synthetic Aperture Radar (InSAR) in detecting surface deformation signals due to wildfire-induced thermokarst over different temporal scales. InSAR has been used to detect long-term and seasonal displacements over several thaw-related landforms in permafrost areas (e.g., Liu et al., 2010, 2014, 2015; Short et al., 2011; Iwahana et al., 2016; Molan et al., 2018; Antonova et al., 2018; Strozzi et al., 2018; Chen et al., 2018). Although subsidence signals as a result of thermokarst associated with Alaskan wildfires have been detected using InSAR (Liu et al., 2014; Iwahana et al., 2016a, 2016b; Molan et al., 2018; Michaelides et al., 2019), no such studies have been conducted on Siberian fires, to our knowledge. Also, all previous InSAR-based post-wildfire deformation mapping has been performed over relatively flat terrains, but no reports over hillslopes have been shown. Moreover, in contrast to previous studies, we employed two independent SAR imageries with distinct carrier frequencies and polarizations, L-band (1.2 GHz) HH- and C-band (5.4 GHz) VV-polarized microwave. Because the imaging geometries were different and had different sensitivities to the 3D displacement vector, we could not only take advantage of the performance of each sensor in mapping deformation signals but could also cross-validate the measurements by two InSAR data sets.

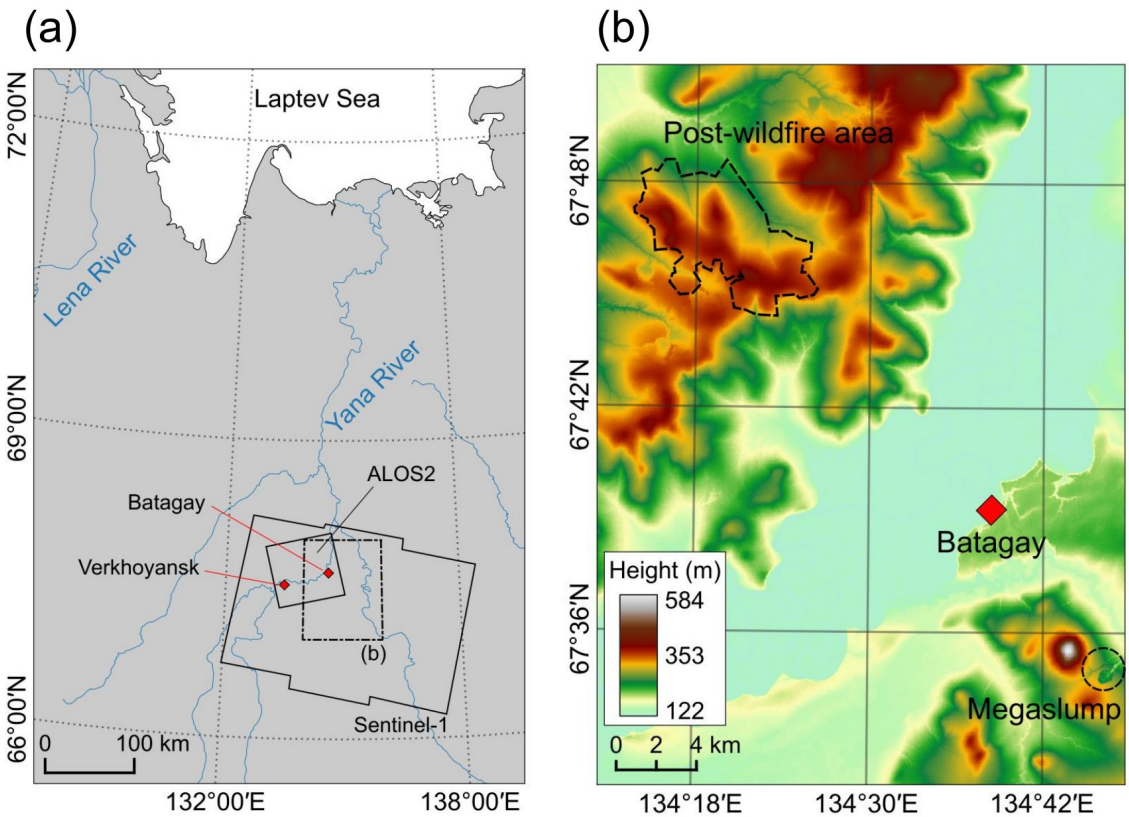

Figure 1. (a) Study area in Eastern Siberia. Black solid line boxes indicate the imaging areas taken by each satellite. Dashed line box indicates the area enlarged in (b). Batagay and Verkhoyansk (red diamonds) are located in the imaging area. (b) Elevation map around Batagay based on a TanDEM-X DEM (12m mesh). The Batagaika megaslump is 15 km southeast of Batagay. Deformation signals due to the wildfire of July 2014 were detected in the black dashed area.

Our second objective was to estimate the cumulative spatial distribution of subsidence, which allows us to estimate the thawed ice volume. Surface deformation signals over permafrost areas have been interpreted as being caused by two major processes: (1) irreversible subsidence due to thawing of ice-rich permafrost or excess ice and (2) seasonally cyclic subsidence and uplift (Liu et al., 2014, 2015; Molan et al., 2018). In these previous reports, however, quality interferograms (InSAR images) were limited in terms of both the temporal coverage and resolution. This limitation existed because the image acquisition interval was 46 days at best and the orbit was not well-controlled in the Japanese Advanced Land Observation Satellite (ALOS) operated from 2006 to 2011 by the Japan Aerospace Exploration Agency (JAXA). For instance, Liu et al (2015) assumed a simple linear subsidence trend in their inversion, probably because of the limitation in temporal coverage. Moreover, the 1.5-year temporal coverage in Molan et al (2018) would be not long enough to resolve the detailed temporal evolution. Hence, the total thawed ice volume estimates were uncertain. We also compared the spatial distribution of subsidence with burn severity and local landform.

Several studies have reported uplift signals by InSAR over permafrost areas (Samsonov et al., 2016; Daout et al., 2017; Chen et al., 2018; Rouyet et al., 2019), but no clear uplift signals have been shown in previous studies at fire scars as interferometric coherence was lost during the freezing season in analyzed areas. In contrast, this study provides the unambiguous detection of upheaval signals in the early freezing season and confirms the absence of continuing uplift during the colder season.

Our third objective was, given the clear frost heave signals, to interpret more physically the observed data. This was because it has been widely accepted that frost heave is unrelated to volume expansion of pre-existing pore water into ice, but caused, instead, by ice lens formation due to the migration of water (Taber, 1929, 1930). However, a physical understanding of frost heave mechanisms has been established only during recent decades (e.g., Dash, 1989; Worster and Wettlaufer, 1999; Rempel et al., 2004, Wettlaufer and Worster, 2006; Dash et al., 2006; Rempel, 2007). Although it appears counter-intuitive, taking a soil particle inside a unit of ice, there exists an unfrozen (premelted) water film between the ice and soil even below the bulk-melting temperature of 0 °C (e.g., Dash, 1989; Worster and Wettlaufer, 1999). Premelted water can be present because of the depression of freezing temperature by the curved geometry of the soil particle and the repulsive inter-molecular force between ice and soil particles. Under a temperature gradient the repulsive thermomolecular pressure on the colder side is greater than on the warmer side. Hence, the net thermo-molecular force on the soil particle tends to move it toward the warmer side, a phenomenon known as thermal regelation (e.g., Worster and Wettlaufer, 1999; Rempel et al., 2004). Meanwhile, the premelted water migrates toward lower temperature, where ice lenses will be formed. These processes are responsible for frost heave and continue as long as the temperature gradient is maintained, or until significant overburden pressure is applied (e.g., Dash, 1989; Worster and Wettlaufer, 1999; Rempel et al., 2004). Although there is still an ongoing debate on the theory (Peppin and Style, 2013), we applied the simple, physics-based 1D theory of Rempel et al (2004) to the observed frost heave signal so that we could physically interpret and explain the observed signals using reasonable parameters.

2 Study Site

Batagay (67°39′30″ N, 134°38′40″ E) is located on the Yana River, which is 872 km long and covers a 238,000 km^2 basin in a part of the East Siberian Lowlands in the Sakha Republic (Figure 1). The elevation ranges between 138 m above sea level at Batagay village and 590 m at Mt. Kirgilyakh on the north-west of Batagaika megaslump (Figure 1b). Our study site was a fire scar located on the western bank of Yana River, with elevation ~200-400 m (Figure 1b).

The climate is highly continental with a mean annual temperature of −15.4 °C and mean annual precipitation 170 – 220 mm (Murton et al., 2017). Meteorological data were sourced from Verkhoyansk, 55 km west of Batagay. The mean temperature for July and December 2017, respectively, was 12 °C and −44 °C, while precipitation was 30 mm and 6 mm, respectively.

We have no in-situ observation data on permafrost conditions and sedimentology before the fire. However, the burned site is approximately 25 km to the northwest of the Batagaika megaslump (Figure 1); thus, we refer to the summary provided by Murton *et al* (2017) as a proxy for basic information on the burned area and permafrost. The open forest is dominated by larch with shrubs and lichen moss ground cover. Using normalized vegetation index by Landsat images we confirmed that the prefire vegetation at the fire scar was almost the same as that around the megaslump. Permafrost in the Yana River valley is continuous with the mean annual ground temperature at the bottom of the active layer, ranging from −5.5 °C to −8.0 °C, with the active layer thicknesses (ALT) beneath the forest/moss cover and open sites being 20-40 cm and 40-120 cm, respectively (Murton et al., 2017). In the upslope at Batagaika megaslump, below the 150 cm thick near-surface sand layer there lies a 20-45 m thick upper ice complex, under which there is a 20-38 m thick lower sand layer. Below this lies a 3-7 m thick lower ice complex (Murton et al., 2017). Although the horizontal distribution of this massive ice complex is yet uncertain, we discuss the possible variations in the ALT in section 5.2.

The wildfire incident occurred in July 2014 over 36 km^2 area, northwest of Batagay (Figure 1). This wildfire event was evident in the Landsat and MODIS optical images taken between July 17 and August 2, 2014. While wildfires in northeastern Siberia are often attributed to human activity (Cherosov et al., 2010), the cause of the July 2014 wildfire is uncertain. The number of days with high flammability has noticeably increased over large parts of Russia, including the Far East (Roshydromet, 2008). For instance, areas near our study site have experienced even larger wildfires in 2019 (Siberian Times, 2019), as well as a smaller wildfire near the Batagaika megaslump in 2018.

3 Methods

3.1 InSAR and Data Sets

InSAR has been used as a technique to detect surface displacements (see Bürgmann et al., 2000; Hanssen, 2001; Simons and Rosen, 2015 for detailed reviews). InSAR can map surface displacements over the swath areas with spatial resolution on the order of 10 m or less. InSAR image, called an interferogram, is derived by taking the differences between the phase values of SAR images at two acquisition epochs and further correcting for the known phases contributed from orbital separation (spatial baseline) and topography. Most SAR satellites have near-polar orbits, transmit microwave pulses normal to the flight direction and illuminate the surface of the Earth in ~50-500 km wide belts depending on satellite type and its observation mode (Figure 1a). The actual InSAR deformation map indicates the radar line-of-sight (LOS) changes that are derived by a projection of the 3D surface displacements onto the LOS direction. Because the incidence angle of the illuminating microwave is ~30°-40°, LOS changes are most sensitive to vertical (up-down) displacement followed by east-west displacement and are least sensitive to north-south displacement because of near-polar orbit. More specifically, the sensitivity to east-west displacement changes sign, depending on whether the surface is illuminated from the east or the west.

Depending on the specific two SAR image pairs and imaged locations, it is not always possible to quantify surface displacements from interferograms. As the phase values of an original interferogram are wrapped into $[-\pi, +\pi]$ with 2π ambiguity, they need to be unwrapped to quantify spatially continuous LOS changes. However, phase unwrapping becomes impossible when the reflected waves received at the two acquisitions lack interferometric coherence (i.e., they are uncorrelated with each other). Lower coherence is caused by long spatial baseline and temporal changes in the scattering characteristics at the SAR image resolution cell (temporal decorrelation). For instance, significant ground cover differences between conditions of deep snow and dry surface cause temporal decorrelation.

Effects of microwave propagation through non-vacuum medium, ionosphere and troposphere, on the derived interferometric phase also need to be considered, as they generate apparent LOS changes that are unrelated to surface displacements. Moreover, recent studies have also reported the effect of soil-moisture changes through volume scattering within the surface soil on the interferometric phase (e.g., De Zan et al., 2014; Zwieback et al., 2015, 2016).

In this study, we used L-band (23 cm wavelength) HH-polarized SAR images derived from the PALSAR-2 acquired by the Japanese Advanced Land Observing Satellite 2 (ALOS2) from 2015 to 2019 together with C-band (5.6 cm wavelength) VV-polarized SAR images taken during 2017-2019 derived from Sentinel-1 (Figure 2; see also Tables 1 and 2 for details). The incidence angles at the center of images were 36° and 39° for ALOS2 and Sentinel-1, respectively. In the data sets used, ALOS2 and Sentinel-1 were illuminating the surface from the west and east, respectively, and thus the sensitivity to the east-west displacement was in reverse. To correct for topographic phases, we used TanDEM-X DEM (12m mesh). Compared to the former ALOS-1/PALSAR-1 InSAR, the ALOS2 orbit is well controlled, and the spatial baseline is much shorter (Table 1), which allowed us to ignore DEM errors in the interferograms; the same is true for Sentinel-1 (Table 2).

Tropospheric delay itself does not depend on the carrier frequency, but C-band InSAR provides more phase changes because of its shorter wavelength. In contrast, L-band InSAR phase is more prone to ionospheric effect, which could be corrected for by range split-spectrum method (Gomba et al., 2016; Furuya et al., 2017). However, the spatial scale of ionospheric anomalies was much larger than that of the burned area, and the ionospheric signals were apparently uncorrelated with the deformation signal. Thus, we simply took out the long-wavelength phase trend by fitting a low-order polynomial with clipped InSAR images after masking out the burned area. We also corrected for topography-correlated tropospheric errors when they clearly appeared in the InSAR image. These procedures were somewhat ad-hoc but allowed us to isolate relative displacements with respect to un-burned areas regarded as reference. It was also likely, however, that possible long-wavelength permafrost degradation signals, known as "isotropic thaw subsidence" (Shiklomanov et al., 2013), were eliminated. Yet, it would be challenging to detect isotropic thaw subsidence signal only from InSAR data. Hence, we simply ignored such possible long-wavelength deformation signals.

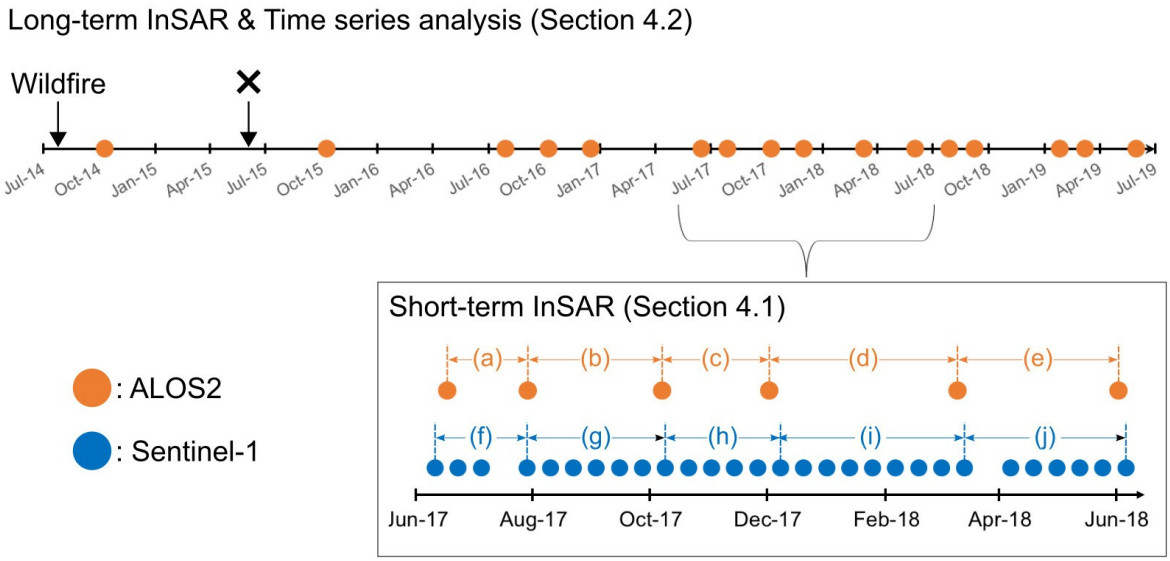

Figure 2. Schematic diagram of data time series. (Top) Long-term changes are derived from ALOS2 acquired on orange dots. Wildfire occurred from July to August 2014, and JAXA modified the center frequency of PALSAR-2 Beam No. F2-6 data in June 2015 shown with the cross. (Bottom) Short-term deformation during 2017-2018 as examined by Sentinel-1 images. We compare the ALOS2 and Sentinel-1 deformation maps during the five periods, (a)—(e) and (f)—(j).

While ALOS2 has only imaged the area since 2014 its data acquisition interval is much longer than that of Sentinel-1 (Figure 2). Previous studies demonstrate that it is not possible to infer the total subsidence using pre- and post-wildfire SAR images, as the drastic changes in land cover cause low interferometric coherence (Liu et al., 2014; Molan et al., 2018). Additionally, JAXA changed the carrier frequency of PALSAR-2 in June 2015 (Figure 2). Hence, monitoring long-term deformation using ALOS2 InSAR is possible only since October 2015. Conversely, frequent data acquisition in Sentinel-1 started only in 2017. Thus, we first performed an inter-comparison between ALOS2 and Sentinel-1 InSAR, focusing on the seasonal changes in 2017. We stacked Sentinel-1 interferograms to set the temporal coverages to nearly identical with those of ALOS2 (Figure 2). Stacking was necessary because we failed to derive long-term Sentinel-1 interferograms, as the burned areas quickly lost coherence. During the temporal interval of ALOS2 images Sentinel-1 had more cycles. Therefore, the number of Sentinel-1 stacks varied from three to eight (Figure 2).

Although L-band SAR is known to have better interferometric coherence than C-band SAR (e.g., Rosen et al., 1996) our study indicated that Sentinel-1 could maintain a comparable interferometric coherence with L-band ALOS2 even during winter season. This is likely due to the short acquisition period of 12 days as well as the somewhat drier snow in the area in winter that allows microwave to reach the ground. A dry snow cover of depth less than 1 m is undetectable to microwave radiation, whereas over wet snow surface scattering dominates (Rees, 2001). The frequent data acquisition of Sentinel-1 since 2017 allowed us to examine detailed seasonal changes in surface deformation (Figure 2). Some Sentinel-1 InSAR pairs in early summer, however, did not show good coherence, possibly due to snow wetness.

In order to infer long-term temporal changes and cumulative displacements, we performed SBAS (Small Baseline Subset)-type time-series analysis (Berardino et al., 2002; Schmidt and Bürgmann, 2003), using 50 high-quality ALOS2 interferograms that included one-year- as well as short-term interferograms (Figure 3). We could estimate the average LOS-change rates between each acquisition epoch without assuming any temporal change models. In contrast to the original SBAS approach, we did not estimate DEM errors because the well-controlled orbit, as well as the precise TanDEM-X DEM, have no sensitivities to those errors.

In order to estimate the errors of the derived time series, we assumed each original SAR scene contained 0.2 cm errors, and made InSAR data covariance matrix, following the method of Biggs et al. (2007). The errors are relatively smaller than those in previous studies of SBAS analysis (e.g. 0.4 cm in Schmidt et al., 2003; 0.75 cm in Biggs et al., 2007), because, as noted earlier, we took out the long-wavelength phase trend form each InSAR image, and the analysis area is smaller (12 ×12 km) than previous studies.

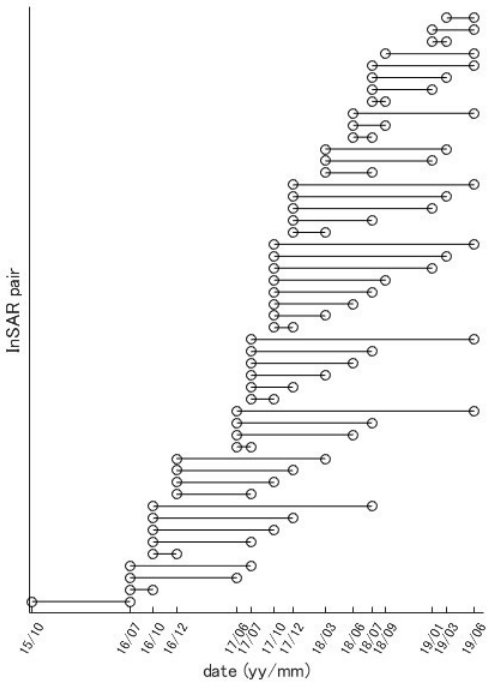

Figure 3. Temporal distribution of interferograms for the time-series analysis. 50 interferograms were generated from 15 ALOS2 SAR images.

3.2 Multispectral remote sensing of burn severity

Normalized burn ratio (NBR) is a useful multispectral remote sensing index to assess the impact of wildfire on vegetation. Vegetation reflects more strongly in the near-infrared (NIR) than in the shortwave infrared (SWIR) region, while a fire scar reflects more strongly in the SWIR. Utilizing this property, NBR is defined as NBR=(NIR−SWIR)/(NIR+SWIR). The difference NBR (dNBR), i.e., the difference between prefire NBR and postfire NBR, indicates burn severity (Key and Benson, 2006; Miller and Thode, 2007). Generally, when dNBR is greater than 0.66 the fire is regarded as “highly severe”. We computed dNBR for the 2014 fire using Landsat 8, Band 5 (850-880 nm) and Band 7 (2110-2290 nm) images for near-infrared and shortwave-infrared, respectively, to associate the inferred subsidence distribution with burn severity.

3.3 One dimensional frost-heave theory based on premelting dynamics

We used the one-dimensional frost-heave theory as a tool to interpret the observed uplift signals. Inspired by one-way frost heave experiments (Mutou et al., 1998; Watanabe and Mizoguchi, 2000), Worster and Wettlaufer (1999) and Rempel et al (2004) derived a steady-state heave rate V_l of an ice lens, considering the force balance among thermo-molecular force F_T, hydrodynamic force F_μ, and overburden force F_O (pressure P_0). Here, we assumed a constant heave rate V_l, which may not necessarily reflect the actual observations shown below as well as in Hu et al (2018). However, this assumption simplified the theory, and we assumed that the observed heave rate did not change drastically over time. Rempel et al (2004) proposed a non-dimensional heave rate v_l of an ice lens as a function of its boundary position ξ_l given:

$$v_l \equiv \frac{\mu V_l}{k_0 \rho G} = \left[\int_0^{\xi_l} \left(1 - \phi S_s\right) d\xi - p_o \right] \left[\int_{\xi_h}^{\xi_l} \frac{\left(1 - \phi S_s\right)^2}{\tilde{k}} d\xi \right]^{-1},$$

where μ, k_0, and ρ are the viscosity of water, the permeability of ice-free soil, density of water, respectively. The quantity $G \equiv \left(L / T_m\right) \langle \nabla T \rangle$ has the same dimension as gravity and indicates thermo-molecular force when multiplied by the mass of displaced ice; L is the latent heat of fusion and T_m is the bulk melting temperature. The first and second term in the bracketed numerator are proportional to F_T and F_O, respectively, while the bracketed denominator is proportional to F_μ. The integral is performed along $\xi \equiv z / z_f$, where z_f is the position above (below) where ice saturation S_s becomes non-zero (zero); z_h indicates the position where hydrostatic pressure is achieved, and ϕ is the porosity of soil. The normalized overburden pressure and permeability are defined as $p_0 \equiv P_0 / \rho G z_f$ and $\tilde{k} \equiv k / k_0 \geq 1$, respectively.

4 Results

We performed an inter-comparison of ALOS2/Sentinel-1 interferograms, focusing on the seasonal changes in surface deformation. We then showed short-term deformation derived by Sentinel-1 and long-term deformation derived by time-series analysis of ALOS-2. Subsequently, we estimated the total volume of thawed excess ice. Although both satellite images covered the Batagaika megaslump we did not observe clear LOS changes as detected at the fire scar, which could be due to the lack of spatial resolution of the InSAR images.

4.1 Seasonal deformation and comparison of ALOS2/Sentinel-1 interferograms

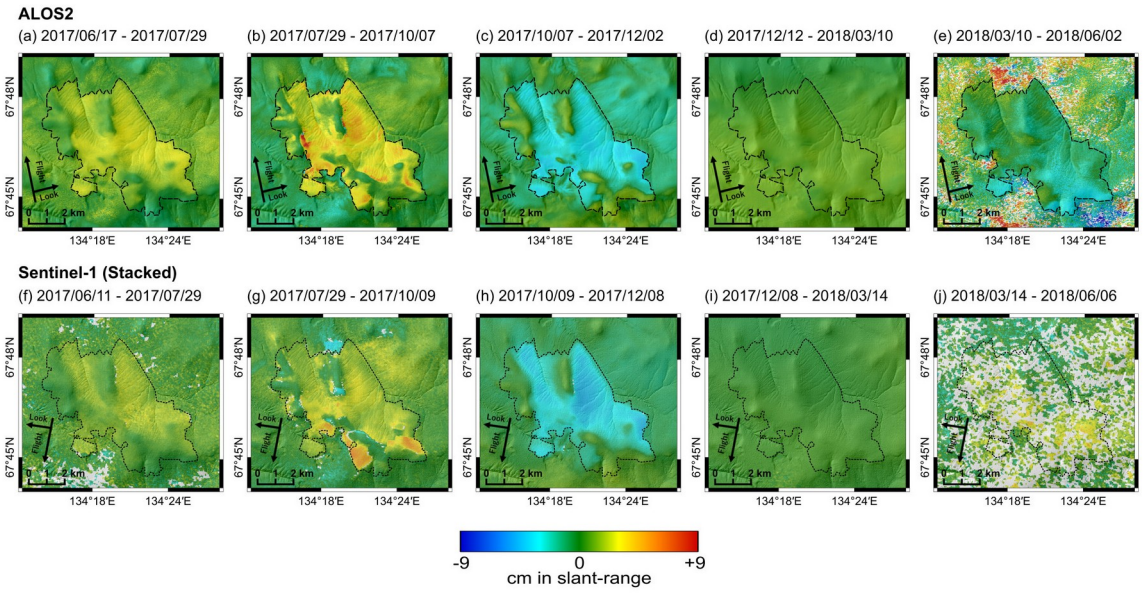

Figure 4. (Top) ALOS2 interferograms during the five periods, (a—e). (Bottom) Sentinel-1 stacked interferograms during the five periods, (f)—(j), derived so that the temporal coverage could nearly match those from (a) to (e); all the interferograms are overlaid on shaded relief maps. Warm and cold colors indicate LOS changes away from and toward the satellite, respectively.

We compared the ALOS2 and stacked Sentinel-1 interferograms for five periods (Figure 4) and assessed their differences (Figure 5). Despite differences in look directions both ALOS2 and Sentinel-1 indicated extensions in the LOS during periods (a, f) from the middle of June to the end of July and (b, g) from the end of July to the early October. Also, their deformation areas and amplitude were mostly consistent, suggesting that LOS changes were largely due to summer subsidence (see section 5.1 below for details). In terms of the spatial distribution of deformation signals, we noticed that the LOS changes over higher-elevation areas such as ridge and peak were insignificant, whereas the boundaries between the burned and unburned areas were clear. The north-western area, however, showed few LOS changes (see section 5.2 for the relationship between LOS changes and burn severity). During the period (c, h) from early October to early December both ALOS2 and Sentinel-1 indicated shortening in the LOS by an approximate 5 cm maximum, and the deformation areas and amplitude were quite similar. This observation presumably indicated frost heave in the early freezing period. In view of the previous three periods, both subsiding and uplifting areas were nearly the same. The following period (d, i) from early December to the middle of March also included the winter season with much colder air temperatures, but we did not observe any significant deformation signals, indicating that frost-heave virtually stopped in early December. While the good interferometric coherence during mid-winter was an unexpected result, we speculate that it could have been due to drier, lower amounts of snowfall.

In the periods (e, j) from the middle of March to early June, both ALOS2 and Sentinel-1 suffered from decorrelation, and we could not identify clear deformation signals. However, in light of Figure 6 below, each of the Sentinel-1 interferograms had overall good coherence with the exception of the data acquired in the middle of May. These observations suggested that the decorrelation may be attributable to the rapid changes on the ground surface during the initiation of the thawing season when the air temperature rises above the freezing point and the active layer begins to thaw.

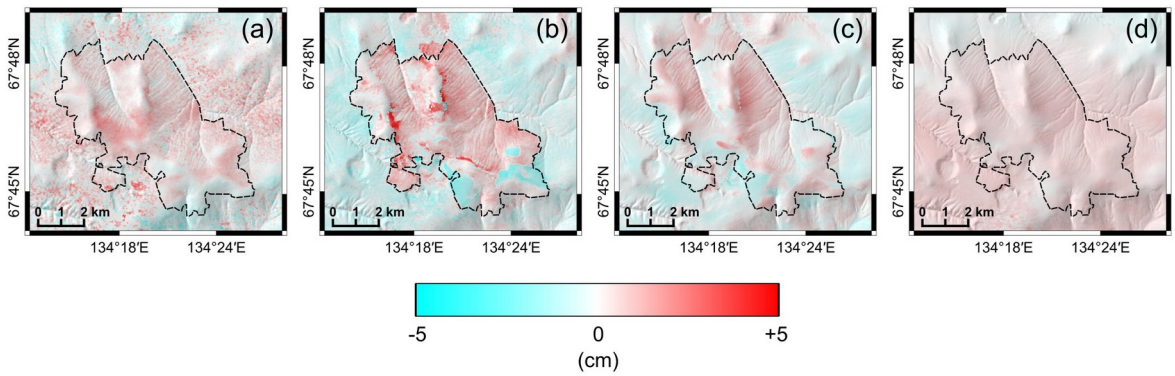

Figure 5. Differences in LOS-change detected by ALOS2 and Sentinel-1 seasonal interferograms (Figures 4a-d and 4f-i). In the last term of seasonal analysis (Figure 4e and 4j), we could not estimate differences due to coherence loss.

Figure 5 shows the differences between ALOS2 and Sentinel-1 InSAR data with nearly identical periods, which may help in cross-validating the measurements and understanding the actual deformation processes. The estimated differences and their 2σ scatter were 0.5±1.2cm (Fig 5a),0.7±2.3cm (Fig 5b),0.3±1.3cm (Fig 5c), and 0.6±0.3cm (Fig 5d), with mean of 0.5±1.5 cm. The differences and their variances were variable over time but apparently indicated some systematic trends. For instance, over the east-facing slopes, the differences were almost always positive (This is discussed more comprehensively in section 5.1).

The Sentinel-1 interferograms for 2017 demonstrate that the progress of deformation was not at a constant rate (Figure 6). The most rapid deformation took place in June (periods 1 and 2) with no substantial deformation in July (period 3) and started to subside again in August (periods 4-6). We found that the subsidence occurred sporadically over time and space and that the burned area did not uniformly subside. For periods 4, 5 and 9 we were unable to perform phase unwrapping at specific locations near the ridge and the boundaries between the burned and unburned areas. These unwrapping errors were responsible for the localized, large differences observed in Figure 5b. We confirmed the presence of low coherence bands along the unwrapping errors, which may suggest large phase jumps due to large displacements during the 12 days; enigmatically, no such line-shaped low coherence was detected in the long-term ALOS2 interferograms. Moreover, Figure 6 demonstrates that the frost heave started in late September, which was missed in the periods (b) and (g) of Figure 4, and that the absence of any deformation signals lasted from early December to May of the following year. We will physically interpret the absence of deformation signals during the coldest season in section 5.3.

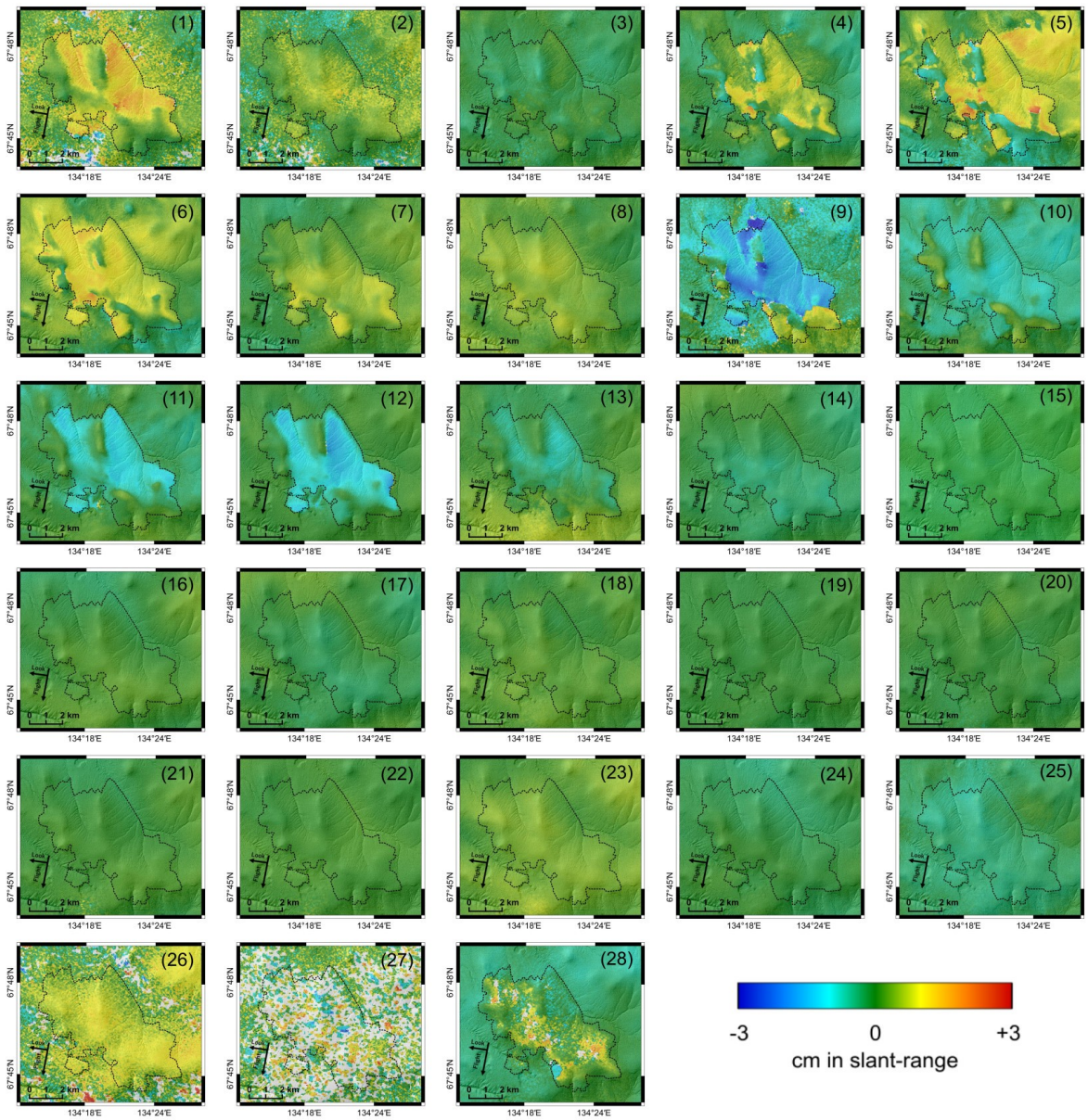

Figure 6. Sentinel-1 interferograms during the 27 periods from June 2017 through June 2018 overlaid on hill-shade map. Details of each image are described in Table 2.

4.2 Long-term deformation inferred from time-series analysis of ALOS2 interferograms

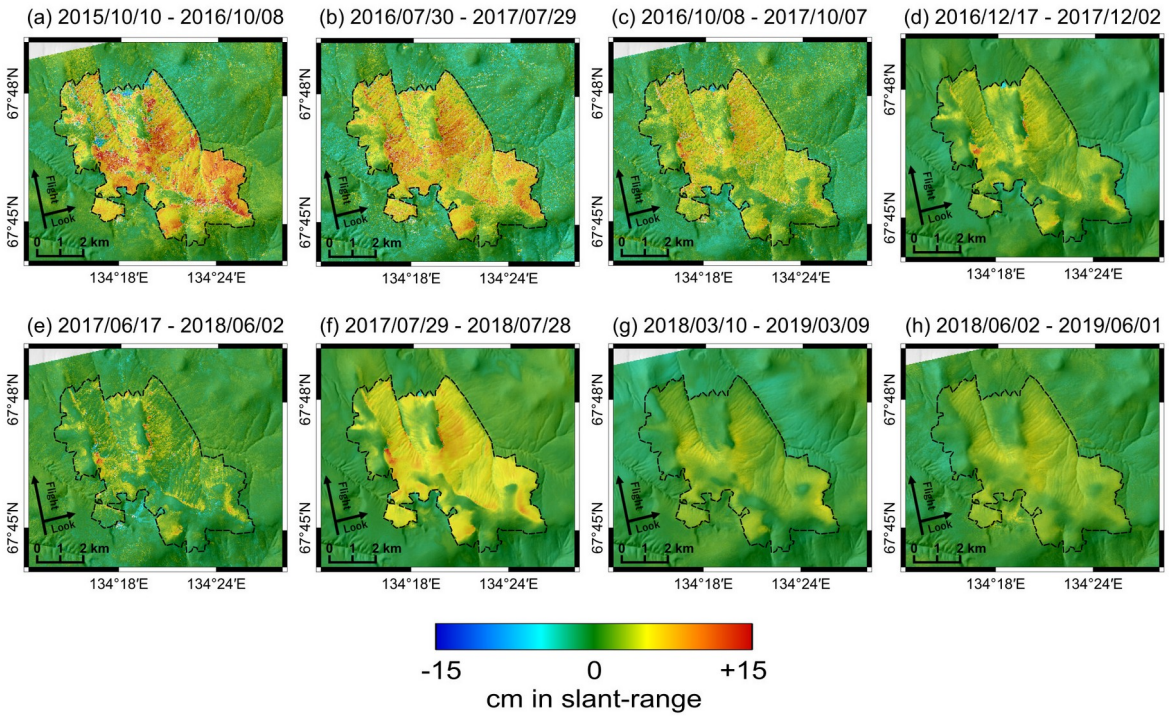

Figure 7. LOS-changes of ALOS2 interferograms overlaid on shaded relief map. Details of each image are described in Table 1; imaging was performed by ascending, right-looking orbit. Warm and cold colors indicate LOS changes away from and toward the satellite, respectively. Black dashed line indicates the boundary between the burned and unburned area confirmed with Landsat optical images.

Figures 7a—7h show ALOS2 interferograms, each of which covers nearly one-year after October 2015 with some overlaps in its temporal coverages. Figure 7a, derived at the earliest period after the fire, indicates the maximum one-year subsidence to be as much as 10 cm or more.

If the amplitude and timing of seasonal subsidence/uplift cycle are invariable over time, a one-year interferogram will tell us only the irreversible displacements regardless of the acquisition times of master/slave images, which corresponds to the “pure ice” model in Liu et al (2015). Figure 7 sequentially shows the periods from October 2015 to June 2019 and indicates that the yearly subsidence rate slowed down. However, the variations of the one-year LOS changes in Figures 7 suggest that the actual deformation processes were more complex.

Figure 8a shows the cumulative LOS changes from October 2015 to June 2019 derived from SBAS-type time-series analysis, and that the maximum LOS extension reached as much as 25 cm; the 2σ errors for Figure 8a were ±1.5cm. Considering that the LOS changes during the first year after the 2014 fire were not included, the total LOS changes were presumably much greater than 25 cm, which meant that the subsidence was greater than 30 cm on account of the 36° incidence angle. As mentioned earlier, however, the higher-elevation areas such as the ridge did not undergo significant deformation, which probably would have been the case even during the first year after the fire. In addition to the high elevation areas, we realized clear contrasts in the LOS changes between the east- and the west-facing slopes near the northwestern area and the central north-south trending ridge; this spatial heterogeneity could also be recognized in Sentinel-1 (Figure 4). Their possible mechanisms comparing the burn severity (Figure 8b) and local landform (Figure 8c) are discussed in section 5.2.

We show the estimated time-series data at four representative sites (Figures 9a-9d), whose locations are indicated in Figure 8a. The sites (a) and (b) underwent nearly the same cumulative LOS changes by roughly 20 cm but were located at different slopes that are 4.3 km apart. On the other hand, the cumulative LOS changes at the site (d) were relatively small (approximately 10 cm). The site (c) located in the ridge did not show either significant seasonal or long-term deformation.

Time series data in Figures 9a and 9b clearly indicate that the largest subsidence took place from 2015 and 2016. We believe, however, that the most significant subsidence probably occurred only during the thaw season in 2016, as we have observed earlier, that no deformation occurred from December to March. Thus, the actual subsidence rate from October 2015 to July 2016 should have been more complicated than that expected from the linear trend in Figures 9a and 9b. The error bars in Figures 9a-9d indicated an estimated standard deviation with 2σ and attained ±1.5cm in the last epoch.

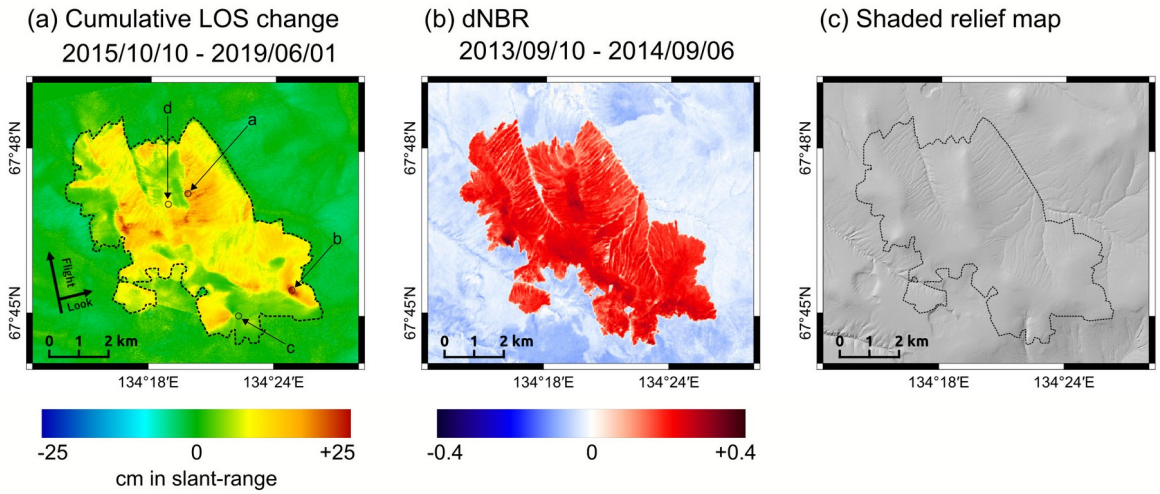

Figure 8. (a) Cumulative LOS changes from 2015 to 2019 estimated by InSAR time-series analysis. The 2σ error is ±1.5cm. The time series of LOS change at each site (a–d) is indicated in Figure 9. (b) Map of dNBR before and after the fire. (c) Shaded relief generated from DEM. Black dashed line indicates the boundary of the 2014 fire.

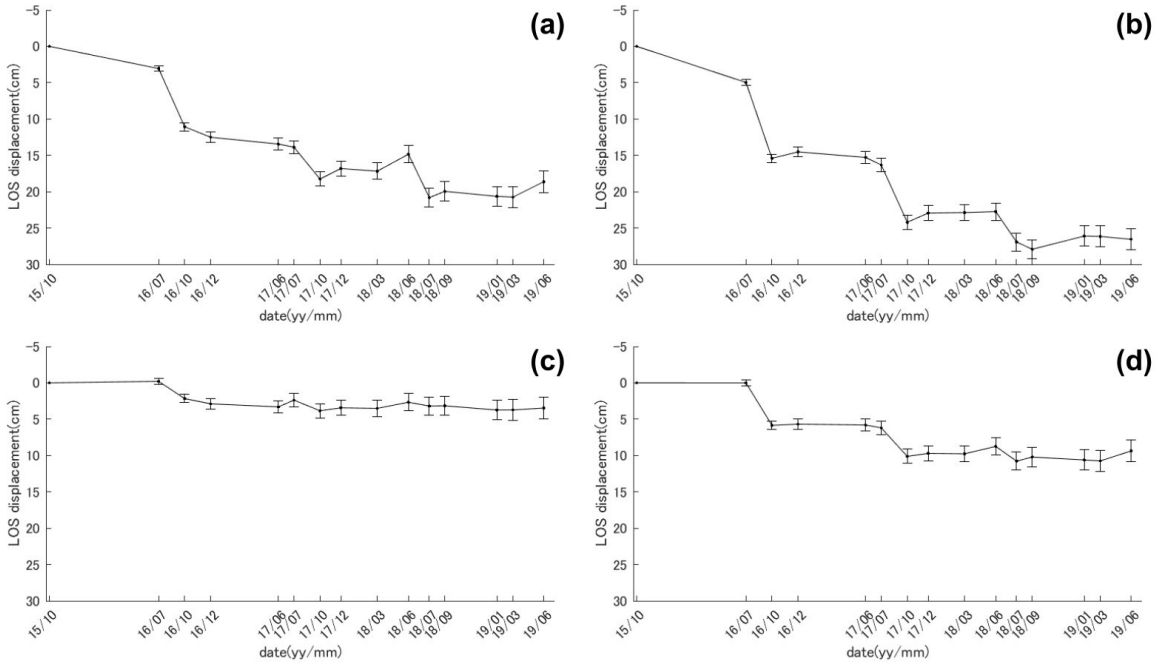

Figure 9. Panels (a–d) indicate the time series of LOS changes at each point indicated in Figure 8. Sites (a) and (b) are located at the east facing slope. Site (c) is located at the ridge, where no deformation signal was detected by original interferograms. Site (d) is at the west facing slope.

4.3 Estimating the total volume of thawed excess ice

Post-wildfire deformation over a permafrost area presumably consists of two contributions: (1) irreversible subsidence due to melting of ice-rich permafrost below the active layer, and (2) seasonally cyclic subsidence and uplift due to freeze-thaw of the active layer (Liu et al., 2014, 2015; Molan et al., 2018). In order to separate the two processes from the observed deformation data, Liu et al (2014) used independent ground-measured ALT data to predict the ALT contribution to total subsidence. Ground-measured pre-fire ALT data were not available at this study site. Given the temporal evolution of post-wildfire deformation data (Figures 9a-9d), however, we may regard the cumulative deformation in Figure 8a as being due to irreversible subsidence during the period between October 2015 and June 2019, and estimate the total thawed volume as $3.56 \pm 2.24 \times 10^6$ m^3; the error bar is based on the root mean square of the no-deformation signals outside the burned area, which is multiplied by the burned area. However, in view of the temporal evolution in Figure 9, we could speculate that a much larger deformation was also taking place immediately after the 2014 fire until October 2015, during which, unfortunately, no deformation data are available. Thus, this estimate should be viewed as a lower estimate, with the actual volume of thawed permafrost possibly being much greater.

Nevertheless, despite its much smaller area size (Figure 1b), the thawed volume at the Batagaika megaslump is greater than 2.5×10^7 m^3 (Günther et al., 2016), an order-of-magnitude larger than our estimate above. Moreover, the thaw-subsidence rate at the fire scar is slowing down (Figure 9). We discuss the possibility of the another megaslump emergence at the fire scar in section 5.2.

5 Discussion

475 5.1 Similarities and differences in the ALOS-2 and Sentinel-1 interferograms: implication for
476 insignificant slope-parallel sliding

477 Taking into account the imaging geometries of the ALOS2 and Sentinel-1, we could
478 comprehensively interpret the differences in Figure 5 and also infer the actual deformation
479 processes. The weights multiplied to the 3D-displacements, (U_{ew}, U_{ns}, U_{ud}), to compute LOS
480 changes were +0.573, +0.132, and −0.809 for ALOS2 and −0.583, +0.236, and −0.777 for
481 Sentinel-1, respectively; eastward, northward and upward displacements were taken to be
482 positive. Assuming the LOS changes of the two sensors are identical (which is roughly the
483 case in Figure 4), and no north-south displacement U_{ns}, the constraint on the east-west and
484 up-down displacements can be derived as U_{ew}:U_{ud} = 0.032:1.156. The assumption of zero U_{ns}
485 might appear unrealistic but can be reasonable over the east- and west-facing slopes, which
486 incidentally cover a broad area of the fire scar. As this constraint indicates the dominance of
487 vertical displacement, we can infer that slope-parallel sliding did not take place over the east-
488 and west-facing slopes.

489 In the thawing season when the vertical displacement is downward (negative), the previous
490 constraint on the two displacements also indicates that the east-west displacement should
491 always be westward (negative), regardless of the slope. As this is physically implausible, we
492 may assume that east-west displacements were virtually zero over both the east- and west-
493 facing slopes. We can thus infer a pure vertical subsidence without any east-west
494 displacements during the thaw season. Hence, the differences between ALOS2 and Sentinel-1
495 in the thawing seasons (Figures 5a and 5b) will be simply equal to $-0.032U_{ud}$. Therefore, we
496 can expect systematically positive differences in the thawing season, regardless of the east-
497 and west-facing slopes, which appear consistent with observations (Figures 5a and 5b).
498 Quantitatively, however, the mean differences of 0.5-0.7 cm are too large to be attributable to
499 the geometric difference alone, on account of the subsidence by as much as 5 cm or more.
500 Here, we hypothesize the possible impact of soil-moisture changes, which can reach ~10 %
501 of the carrier wavelength (Zwieback et al., 2015, 2016). As changes in soil moisture generate
502 larger apparent LOS changes in L-band than in C-band InSAR, the observed differences can
503 be likely.

504 In contrast to thaw subsidence frost-heave is more likely to occur towards the slope normal
505 direction. Assuming the magnitude of slope-normal uplift, U_f, over a slope with gradient θ,
506 the differences between ALOS2 and Sentinel-1 would be $U_f(1.156 \sin\theta - 0.032\cos\theta)$
507 assuming zero U_{ns}. We estimated $|\theta|$=1.58°, which corresponds to 55 m height difference over
508 2 km horizontal distance and was fairly consistent with the slope of the studied area.
509 Meanwhile, the differences can also be considered $1.156U_{ew} - 0.032U_{ud}$, which indicates
510 additional positive and negative effects on the east- and west-facing slope, respectively.
511 Indeed, Figure 5c appears to depict clearer contrasts in sign on the east- and west-facing
512 slopes. Moreover, the impact of changes in soil moisture are likely much smaller in the colder
513 season than in the thaw season, which may explain the smaller differences in freezing
514 seasons.

515 As we derived the differences over the no-deformation season (Figure 5d), we can attribute
516 them to the atmospheric effect on ALOS2 and Sentinel-1 interferogram (Figures 4d and 4i).
517 The overall positive differences are likely because the spatial scale of atmospheric delay was
518 greater than the fire scar area.

519 Previous reports of thermokarst subsidence after fire have focused on relatively flat areas as
520 those at the 2002 tundra fire in the central Seward Peninsula, Alaska (Iwahana et al., 2016b),
521 the 2007 Anaktuvuk River tundra fire (Liu et al., 2014; Jones et al., 2015; Iwahana et al.,
522 2016a), and the 2009 Big Creek Fire in the Alaskan Yukon River basin (Molan et al., 2018).
523 As such, in addition to the broad subsidence detected by InSAR, polygonal patterns
524 associated with ice wedge degradation became clearly visible 4-7 years after the fire by high-
525 resolution optical and LiDAR remote sensing (Jones et al., 2015; Iwahana et al., 2016b). At
526 the studied hillslopes, in contrast, no such polygonal patterns are likely to be detected.
527 Nonetheless, the dominance of vertical displacements with little slope-parallel sliding
528 indicate that rapid active-layer detachment sliding (ALDS) events were insignificant. In
529 contrast, many ALDS events triggered by fire have been mapped at Mackenzie Valley,
530 Canada, whose length could sometimes reach hundreds of meters (Lewkowicz and Harris,
531 2005). If ALDS event with such length occurred, we could have observed significant loss of
532 interferometric coherence. It is possible, however, that local ALDS events occurred but were
533 undetected because of the coarse resolution (~10 m) of InSAR images. Because the
534 subsidence was caused by thawing of ice-rich permafrost, meltwater should have been
535 supplied at the base of active layer. Considering the mechanisms of ALDS (Lewkowicz,
536 2007), porewater pressure increase might have been not enough to reduce the effective
537 overburden stress and to initiate significant slope-parallel sliding. This is possibly because the
538 meltwater could have drained through the gullies. However, in view of the significant uplift
539 signals over the burned area even years after the fire, the meltwater is still likely to be
540 undrained on the slope. If there were further enough water input by, for instance, warmer
541 days and/or heavy rain, significant ALDS events may take place in the future.

542 5.2 What controls the heterogeneous distribution of subsidence magnitude? Possible
543 emergence of another megaslump

544 The cumulative subsidence magnitude was spatially variable but showed some systematic
545 changes. In addition to the ridges and peaks the west-facing slopes showed significantly
546 smaller subsidence than the east-facing slopes (Figures 4 and 8a). To interpret the spatially
547 heterogeneous subsidence, we associated burn severity and local landform with the
548 cumulative subsidence (Figure 8). In light of the inferred dNBR (Figure 8b), which ranged
549 from 0.2 to 0.4, the burn severity was moderate rather than high. Also, the burn severities
550 were spatially less heterogeneous than those of cumulative subsidence and local landform. In
551 fact, we could even identify deformation-free areas having even higher burn severity. Thus,
552 although the fire undoubtedly initiated the subsidence, the burn severity did not control the
553 subsequent cumulative magnitude.

Notably, however, gullies were clearly more developed on the east-facing slopes than on the west-facing slopes (Figure 8c), which were confirmed to be present at least back in 1991 by Landsat image. Considering the striking correlation between the development of gullies and the larger subsidence, there is high likelihood of a causal relationship between them. Similar dependence on the slope aspect was reported by Lacelle et al (2010, 2015), who found that hillslope thaw slumps in the Richardson Mountains–Peel Plateau, northwest Canada, predominantly developed on the east-facing slope. Lacelle et al (2015) interpreted that the active layer on the east-facing slope might be thinner because of lower amount of insolation than on the south- and west-facing slopes, which promoted a triggering mechanisms of thaw slumps because the ice-rich permafrost was closer to the surface. Although the broadly subsiding areas are not so-called thaw slumps, thinner active layers on the east-facing slope are likely and can consistently explain both the larger subsidence and the rich development of gullies. This hypothesis can be tested either by examining the surface deformations at the 2018 and 2019 fire scars and other fire scars across Siberia and other boreal regions or by performing field-based thaw-depths measurement.

The recent slowdown of the subsidence rate (Figure 9) may suggest that the 2014 fire scar could stabilize in the near future. However, although it depends on how quickly the vegetation is recovered, we do not preclude the possible emergence of another megaslump particularly on the east-facing slopes. In order to initiate thaw slumps, ice-rich permafrost needs to be exposed at the surface (Kokelj and Jorgenson, 2013), at which the initial headwall and slump floor are formed. In contrast to the thaw slumps near shorelines, coastlines and riverbanks (e.g., Burn and Lewkowicz, 1990; Kokelj et al., 2009), no mechanical erosions by waves and currents are effective on hillslopes like the studied area. For the development of retrogressive thaw slumps (RTS) on hillslopes, Lacelle et al. (2010) suggested that ALDS triggered by meteorological events could remove the overlying active layer and expose the ice-rich permafrost. Although no large-scale ALDS events were detected during the studied period, they might take place as discussed in the previous section. Moreover, Figure 8a indicates that the subsidence magnitude becomes larger toward upslope, and there are clear boundaries between the subsiding and non-subsiding portions, where an initial headwall for RTS could be exposed. Once an initial headwall has formed, subsequent retreat rate is rapid on the order of several meters per year (Burn and Lewkowicz, 1990; Lacelle et al., 2015). Thus, in order to monitor the early formation process of RTS in more detail, long-term radar remote sensing with higher spatial and temporal resolution would be necessary and promising.

5.3 Interpretation of frost-heave signals

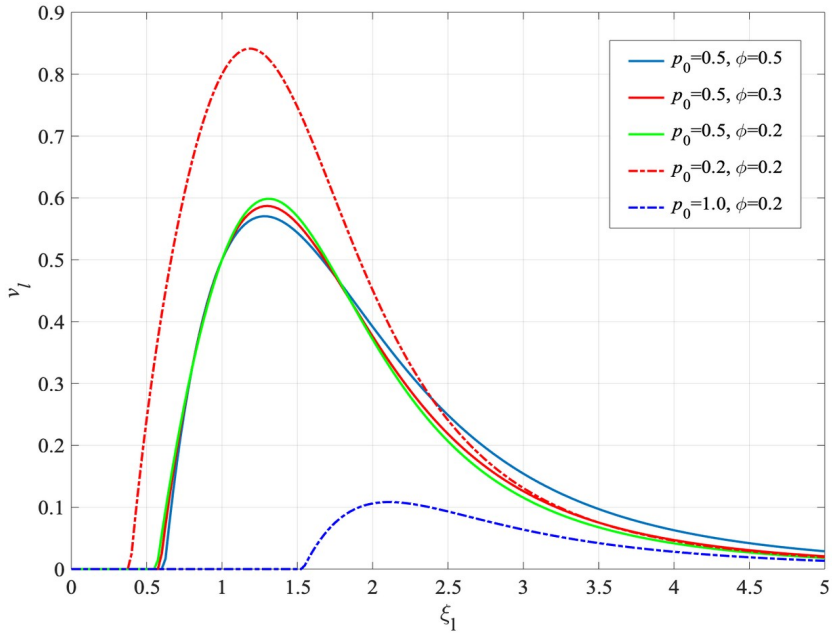

Figure 10. Non-dimensional heave rate profiles of an ice lens as a function of its boundary position, based on the analytical model by Rempel et al (2004). Five cases of non-dimensional overburden pressure p_0 and porosity ϕ are shown.

In order to interpret the detected frost heave signal on the basis of the theory by Rempel et al (2004), we first examine the sensitivity of the heave rate on the normalized overburden pressure p_0 and porosity ϕ. Figure 10 shows five cases of non-dimensional heave rate profiles as a function of the ice lens boundary position ξ_l, indicating that the maximum heave rate is mainly controlled by the normalized overburden pressure p_0 and is somewhat insensitive to the porosity ϕ. Details of the heave rate profiles will depend on the assumed models of permeability and ice saturation, but the qualitative characteristics are not altered (Rempel et al., 2004). There exist two positions that give the same heave rate, but only the branch with smaller ξ_l is stable (Worster and Wettlaufer, 1999; Rempel et al., 2004).

We can attribute the clear contrast in the frost heave signals inside and outside the burned area to the differences in the normalized overburden pressure p_0. Because the mechanical overburden pressure P_0 will not significantly differ from the inside to the outside of the burned area, the larger frost heave rate in the burned area would be caused by larger temperature gradient G and/or deeper frozen depth z_f. Owing to the removal of vegetations and surface organic layers over the burned area, the larger temperature gradient G than that of the unburned area is likely more marked in the early freezing season and may generate a greater thermomolecular force that will effectively reduce the normalized overburden pressure. We may also interpret the absence of frost heave signals in mid-winter as due, probably, to the smaller temperature gradient G than that in late fall/early winter; if frost heave were controlled by temperature instead of temperature gradient, we would expect even more significant signals during the much colder part of the season. The deeper frozen depth z_f is also likely due to the loss of surface vegetation and should supply more water for frost heave.

From the end of September to the middle of November 2017, Figure 6 shows LOS changes by approximately 1.5 cm over 12 days toward the satellite that corresponds to an approximate 1.9 cm uplift. Assuming a constant-rate frost heave, this corresponds to a heave rate of 1.8×10^{-8} (m/s). The most critical parameter controlling heave rate is the permeability for ice-free soil k_0, which can vary by orders-of-magnitude, while other parameters are well-constrained. We may fit our observed heave rate with the ice-free permeability, $k_0 \sim 10^{-17}$ (m^2), which is a likely value in view of the three cases in Rempel (2007).

Here we comment on the modeling of uplift signals as caused by in situ freezing of pore water into ice (Hu et al., 2018). The in situ freezing model is simple, and can explain the timing, duration, and magnitude of uplift signals, if one assumes such pore water in the active layer. However, because the Stefan function approach in Hu et al (2018) is essentially controlled by atmospheric (or ground) temperature that is rather homogeneous over this spatial scale, it is difficult to account for the observed heterogeneous distribution of uplift signals. The distribution of uplift signals was closely correlated with that of subsiding signals, which led us to interpret that the permafrost thaw and its incomplete drainage could become a water reservoir for ice lens formation and frost-heave. The frozen pore ice within the soil and the ice lens formed by water migration are totally different in terms of their formation mechanisms and subsequent forms of ice. From a geomorphological perspective, the presence of ice lenses will play a role in reducing the strength of soil and potentially initiating ALDS, because porewater pressure will increase at the front of thawing, whereas pore ice within the soil would simply stay as pore water with little impact on the landform.

We also recognize, however, that the microphysics-based theory adopted in this study is developed in 1-D geometry and is based on the assumption of "frozen fringe", a region where liquid freezes into ice through the pores of soil. Some laboratory experiments did not support the presence of frozen fringe (e.g., Watanabe and Mizoguchi, 2000), and the "fringe free" frost heave theory has also been proposed; see Peppin and Style (2013) for review. In addition to the controlled lab experiments and theoretical developments, more detailed observations of natural frost heave signals are becoming possible and might help better understand the physics of frost heave and its geomorphological consequences.

6 Conclusions

We used L-band and C-band InSAR to detect post-wildfire ground deformation at Batagay in Sakha Republic, showing not only subsidence signal during the thawing season, but also uplift during the early freezing season and virtually no deformation in midwinter without loss of coherence. Time series analysis allowed us to estimate cumulative displacements and their temporal evolution, as quality interferograms could be obtained even in the winter season. We found that the thawing of permafrost in the burned area lasted three years after the fire, but apparently slowed down after five years. During the studied period, no significant slope-parallel sliding was detected, and the post-wildfire deformation was mostly subsidence. Despite the rather homogeneous burn severity, the cumulative subsidence magnitude was larger on the east-facing slopes and showed a clear correlation with the development of gullies, suggesting that the east-facing active layers might have been originally thinner. Short-term interferograms (2017–2018) indicated that the subsidence and uplift was clearly enhanced compared with the unburned site. We have thus interpreted the frost heave signals within a framework of premelting dynamics. Post-wildfire areas are a focus of permafrost degradation in the Arctic region.

Acknowledgments, Samples, and Data

This study is supported by Researcher's Community Support Projects of Japan Arctic Research Network Center in 2016-2019, and by KAKENHI (19K03982). PALSAR2 level 1.1 data are provided by the PALSAR Interferometry Consortium to Study our Evolving Land Surface (PIXEL) and the ALOS2 RA6 project (3021) under cooperative research contracts with the JAXA. Sentinel-1 SLC data are freely available. TanDEM-X DEM copyrighted by DLR and were provided under TSX proposal DEM_GLAC1864. Climate data at Verkhoyansk, Russia, are available from ClimatView site; http://ds.data.jma.go.jp/tcc/tcc/products/climate/climatview/outline.html. We thank Go Iwahana for discussing our preliminary results. We also acknowledge Lin Liu, two anonymous reviewers and the editors, Joel B. Sankey and Amy East, for their extensive and constructive comments, which were helpful in improving the original manuscript.

References

Antonova, S., Sudhaus, H., Strozzi, T., Zwieback, S., Kääb, A., Heim, B., Langer, M., Bornemann, N., & Boike, J. (2018). Thaw Subsidence of a Yedoma Landscape in Northern Siberia, Measured In Situ and Estimated from TerraSAR-X Interferometry. *Remote Sensing*, 10(4):494, doi:10.3390/rs10040494.

Berardino, P., Fornaro, G., Lanari, R., & Sansosti, E. (2002). A New Algorithm for Surface Deformation Monitoring Based on Small Baseline Differential SAR Interferograms, *IEEE Trans. Geosci. Remote Sens.*, 40(11), 2375—2383. doi:10.1109/TGRS.2002.803792

Biggs, J., Wright, T., Lu, Z., & Parsons, B. (2007). Multi-interferogram method for measuring interseismic deformation: Denali Fault, Alaska. *Geophys. J. Int.*, 170(3), 1165–1179. doi:10.1111/j.1365-246X.2007.03415.x.

Burn, C. R., & Lewkowicz A. G. (1990). Retrogressive thaw slumps. *The Canadian Geographer*, 34, 273–276.

Chen, J., Günther, F., Grosse, G., Liu, L., & Lin, H. (2018). Sentinel-1 InSAR Measurements of Elevation Changes over Yedoma Uplands on Sobo-Sise Island, Lena Delta. *Remote Sensing*, 10, 1152; doi:10.3390/rs10071152.

Chen, J., Liu, L., Zhang, T., Cao, B., & Lin, H. (2018). Using Persistent Scatterer Interferometry to Map and Quantify Permafrost Thaw Subsidence: A Case Study of Eboling Mountain on the Qinghai−Tibet Plateau. *J. Geophys. Res., Earth Surf.*, 123(10), 2663-2676, doi:10.1029/2018JF004618.

Cherosov, M. M., Isaev, A.P., Mironova, S.I., Lytkina, L.P., Gavrilyeva, L.D., Sofronov, R.R., Arzhakova, A.P., Barashkova, N.V., Ivanov, I.A., Shurduk, I.F., Efimova, A.P., Karpov, N.S., Timofeyev, P.A., & Kuznetsova, L.V. (2010). Vegetation and human activity, in The Far North Plant Biodiversity and Ecology of Yakutia, edited by A. P. Isaev et al., 286 pp., Springer, New York.

Daout, S., Doin, M. P., Peltzer, G., Socquet, A., & Lasserre, C. (2017). Large−scale InSAR monitoring of permafrost freeze−thaw cycles on the Tibetan Plateau. *Geophys. Res. Lett.*, 44(2), 901-909, doi:10.1002/2016GL070781.

Dash, J. G. (1989). Thermomolecular Pressure in Surface Melting: Motivation for Frost Heave, *Science*, 246, 1591-1593.

703 Dash, J. G., Rempel, A. W., & Wettlaufer, J. S. (2006). The physics of premelted ice and its
704 geophysical consequences, *Rev. Mod. Phys.*, 78, 695—741.
705 doi:10.1103/RevModPhys.78.695.

706 De Zan, F., Parizzi, A., Prats-Iraola, P., & Lopez-Dekker, P. (2014). A SAR interferometric
707 model for soil moisture, *IEEE Trans. Geosci. Remote Sens.*, 52(1), 418–425. doi:
708 10.1109/TGRS.2013.2241069.-

709 Furuya, M., Suzuki, T., Maeda, J., & Heki, K. (2017). Midlatitude sporadic-E episodes
710 viewed by L-band split-spectrum InSAR, *Earth Planets Space*, 69:175.
711 doi:10.1186/s40623-017-0764-6.

712 Gibson, C. M., Chasmer, L. E., Thompson, D. K., Quinton, W. L., Flannigan, M. D., &
713 Olefeldt, D. (2018). Wildfire as a major driver of recent permafrost thaw in boreal
714 peatlands, *Nature Comm*., 9:3041, doi:10.1038/s41467-018-05457-1.

715 Gomba, G., Parizzi, A., Zan, F. D., Eineder, M., & Bamler, R. (2016). Toward operational
716 compensation of ionospheric effects in SAR interferograms: The split-spectrum
717 method, *IEEE Trans. Geosci. Remote Sens.*, 54 (3), 1446–1461.
718 doi:10.1109/TGRS.2015.2481079

719 Günther, F., Grosse, G., Jones, B. M., Schirrmeister, L., Romanovsky, V. E., & Kunitsky, V.
720 V. (2016). Unprecedented permafrost thaw dynamics on a decadal time scale: Batagay
721 mega thaw slump development, Yana Uplands, Yakutia, Russia, AGU Fall Meeting
722 San Francisco, USA, 12 December 2016 - 16 December 2016.

723 Hinkel, K. M. & Hurd, J. K. Jr. (2006). Permafrost Destabilization and Thermokarst
724 Following Snow Fence Installation, Barrow, Alaska, U.S.A., AAAR, 38(4), 530-539.

725 Hu, F. S., Higuera, P. E., Walsh, J. E., Chapman, W. L., Duffy, P. A., Brubaker, L. B., &
726 Chipman, M. L. (2010). Tundra burning in Alaska: linkages to climatic change and
727 sea ice retreat. *J. Geophys. Res. Biogeosci*. 115, G04002, doi:10.1029/2009JG001270.

728 Hu, Y., Liu, L., Larson, K. M., Schaefer, K. M., Zhang, J., & Yao, Y. (2018). GPS
729 Interferometric Reflectometry reveals cyclic elevation changes in thaw and freezing
730 seasons in a permafrost area (Barrow, Alaska), *Geophys. Res. Lett*., 45, 5581, doi:
731 10.1029/2018GL077960.

732 Iwahana, G., Uchida, M., Liu, L., Gong, W., Meyer, F. J., Guritz, R., Yamanokuchi, T., &
733 Hinzman, L. (2016a). InSAR Detection and Field Evidence for Thermokarst after a
734 Tundra Wildfire, Using ALOS-PALSAR, *Remote Sensing*, 8, 218,
735 doi:10.3390/rs8030218.

736 Iwahana, G., Harada, K., Uchida, M., Tsuyuzaki, S., Saito, K., Narita, K., Kushida, K., &
737 Hinzman, L. D. (2016b). Geomorphological and geochemistry changes in permafrost
738 after the 2002 tundra wildfire in Kougarok, Seward Peninsula, Alaska, *J. Geophys.
739 Res., Earth Surf.*, 115(3), 1–14, doi.org/10.1002/2016JF003921

740 Jafarov, E. E., Romanovsky, V. E., Genet, H., McGuire, A. D., & Marchenko, S. S. (2013).
741 The effects of fire on the thermal stability of permafrost in lowland and upland black
742 spruce forests of interior Alaska in a changing climate, *Environ. Res. Lett*., 8, 035030,
743 doi:10.1088/1748-9326/8/3/035030.

744 Jones, B. M., Grosse, G., Arp, C. D., Miller, E., Liu, L., Hayes, D. J., & Larsen, C. F. (2015).
745 Recent Arctic tundra fire initiates widespread thermokarst development, *Sci. Rep*. 5,
746 15865; doi: 10.1038/srep15865.

747 Jorgenson, M. (2013). Thermokarst terrains, in Treatise on Geomorphology, vol. 8, edited by
748 J. Shroder, R. Giardino, and J. Harbor, chap. Glacial and Periglacial Geomorphology,
749 pp. 313–324, Academic Press, San Diego, Calif.

750 Kanevskiy, M., Shur, Y., Fortier, D., Jorgenson, M.T. & Stephani, E. (2011).
751 Cryostratigraphy of late Pleistocene syngenetic permafrost (yedoma) in northern
752 Alaska, Itkillik River exposure. *Quaternary Research*, 75(3), 584-596, doi:
753 10.1016/j.yqres.2010.12.003.

754 Kasischke, E., & Turetsky, M. (2006). Recent changes in the fire regime across the North
755 American boreal region-spatial and temporal patterns of burning across Canada and
756 Alaska, *Geophys. Res. Lett.,* 33, L09703, doi:10.1029/2006GL025677.

757 Kokelj, S. V., & Jorgenson, M. T. (2013). Advances in Thermokarst Research, *Permafr.*
758 *Periglac. Process*., 24, 108–119, doi: 10.1002/ppp.1779.

759 Kunitsky, V. V., Syromyatnikov, I. I., Schirrmeister, L., Skachk-ov, Y. B., Grosse, G.,
760 Wetterich, S. & Grigoriev, M.N. (2013). Ice-rich permafrost and thermal denudation
761 in the Batagay area - Yana Upland, East Siberia, *Kriosfera Zemli* (Earth' Cryosphere),
762 17(1), 56-68. (in Russian)

763 Lacelle, D., Bjornson, J., & Lauriol, B. (2010). Climatic and Geomorphic Factors Affecting
764 Contemporary (1950–2004) Activity of Retrogressive Thaw Slumps on the Aklavik
765 Plateau, Richardson Mountains, NWT, Canada. *Permafr. Periglac. Process*., 21, 1–15,
766 doi: 10.1002/ppp.666.

767 Lacelle, D., Brooker, A., Fraser, R. H., & Kokelj, S. V. (2015). Distribution and growth of
768 thaw slumps in the Richardson Mountains–Peel Plateau region, northwestern Canada.
769 *Geomorphology*, 235, 40-51, doi:10.1016/j.geomorph.2015.01.024

770 Lewkowicz, A. G., & Harris, C. (2005). Morphology and geotechnique of active-layer
771 detachment failures in discontinuous and continuous permafrost, northern Canada.
772 *Geomorphology*, 69, 275-297, doi:10.1016/j.geomorph. 2005.01.01

773 Lewkowicz, A. G. (2007). Dynamics of active- layer detachment failures, Fosheim Peninsula,
774 Ellesmere Island, Nunavut, Canada. *Permafr. Periglac. Process*., 18, 89–103, doi:
775 10.1002/ppp.578.

776 Liu, L., Zhang, T., & Wahr, J. (2010). InSAR measurements of surface deformation over
777 permafrost on the North Slope of Alaska. *J. Geophys. Res., Earth Surf.*, 115(3), 1–14,
778 doi.org/10.1029/2009JF001547

779 Liu, L., Jafarov, E. E., Schaefer, K. M., Jones, B. M., Zebker, H. A., Williams, C. A., Rogan,
780 J. & Zhang, T. (2014). InSAR detects increase in surface subsidence caused by an
781 Arctic tundra fire, *Geophys. Res. Lett.*, 41, 3906–3913, doi:10.1002/2014GL060533.

782 Liu, L., Schaefer, K. M., Chen, A. C., Gusmeroli, A., Zebker, H. A., & Zhang, T. (2015).
783 Remote sensing measurements of thermokarst subsidence using InSAR, *J. Geophys.*
784 *Res., Earth Surf*., 1935–1948, doi:10.1002/2015JF003599.

785 Mack, M., Bret-Harte, M., Hollingsworth, T., Jandt, R. R., Schuur, E. A. G., Shaver, G. R., &
786 Verbyla, D. L. (2011). Carbon loss from an unprecedented Arctic tundra
787 wildfire, *Nature,* 475, 489–492, doi:10.1038/nature10283.

788 Michaelides, R. J., Zebker, H. A., Schaefer, K., Parsekian, A., Liu, L., Chen, J., Natali, S.,
789 Ludwig, S., & Schaefer, S. (2019). Inference of the impact of wildfire on permafrost
790 and active layer thickness in a discontinuous permafrost region using the remotely
791 sensed active layer thickness (ReSALT) algorithm, *Environ. Res. Lett*., 14(3), 035007.

792 Murton, J. B., Edwards, M. E., Lozhkin, A. V., Anderson, P. M., Savvinov, G. N., Bakulina,
793 N., Bondarenko, O. V., Cherepanovah, M. V., Danilov, P. P., Boeskorov, V., Goslar, T.,
794 Grigoriev, S., Gubin, S. V., Korzun, J. A., Lupachev, A. V., Tikhonov, A., Tsygankova,
795 V. I., Vasilieva, G. V., & Zanina, O. G. (2017). Preliminary paleoenvironmental
796 analysis of permafrost deposits at Batagaika megaslump, Yana Uplands, northeast
797 Siberia, *Quaternary Res.*, 87, 314–330, doi:10.1017/qua.2016.15.

798 Mutou, Y., Watanabe, K., Ishizaki, T. & Mizoguchi, M. (1998). Microscopic observation of
799 ice lensing and frost heave in glass beads. In *Proc. Seventh Intl. Conf. on Permafrost*,
800 June 23–27, 1998, Yellowknife, Canada (ed. A. G. Lewkowicz & M. Allard), pp. 283–
801 287. Universite Laval, Montreal, Canada.

802 Molan, Y. E., Kim, J. W., Lu, Z., Wylie, B., & Zhu, Z. (2018). Modeling Wildfire-Induced
803 Permafrost Deformation in an Alaskan Boreal Forest Using InSAR Observations,
804 *Remote Sens.*, 10, 405; doi:10.3390/rs10030405.

805 Peppin, S. S. L., & Style, R. W. (2013). The Physics of Frost Heave and Ice-Lens Growth,
806 *Vadose Zone J.*, 12, 1-12, doi:10.2136/vzj2012.0049

807 Rees, W. G. (2001). Physical Principles of Remote Sensing, Cambridge University Press,
808 Cambridge, United Kingdom.

809 Rempel, A. W., Wettlaufer, J. S. & Worster, M. G. (2004). Premelting dynamics in a
810 continuum model of frost heave, *J. Fluid. Mech.*, 498, 227-224; doi:
811 10.1017/S0022112003006761

812 Rempel, A. W. (2007). Formation of ice lenses and frost heave, *J. Geophys. Res., Earth Surf.*,
813 112, F02S21, doi:10.1029/2006JF000525.

814 Rosen, P. A., Hensley, S., Zebker, H. A., Webb, F. H., & Fielding, E. J. (1996). Surface
815 deformation and coherence measurements of Kilauea Volcano, Hawaii, from SIR−C
816 radar interferometry, *J. Geophys. Res., Planets*, 101(E10), 23,109—23,125,
817 doi:10.1029/96JE01459.

818 Roshydromet (2008). Assessment report on climate change and its consequences in Russian
819 Federation – General Summary. Moscow.
820 http://climate2008.igce.ru/v2008/pdf/resume_ob_eng.pdf

821 Rouyet, L., Lauknes, T. R., Christiansen, H. H., Strand, S. M., & Larsen, Y. (2019). Seasonal
822 dynamics of a permafrost landscape, Adventdalen, Svalbard, investigated by InSAR.
823 *Remote Sens. Environ.*, 231, 111236, doi:10.1016/j.rse.2019.111236.

824 Samsonov, S. V., Lantz, T. C., & Kokelj, S. V. (2016). Growth of a young pingo in the
825 Canadian Arctic observed by RADARSAT-2 interferometric satellite radar. *The*
826 *Cryosphere,* 10(2), 799, doi:10.5194/tc-10-799-2016.

827 Schirrmeister, L., Froese, D., Tumskoy, V., Grosse, G., & Wetterich, S. (2013). Yedoma: Late
828 Pleistocene Ich-Rich Syngenetic Permafrost of Beringia, in *Encyclopedia of Quart.*
829 *Sci*., 3, 542-552.

830 Schmidt, D. A. & Bürgmann, R. (2003). Time-dependent land uplift and subsidence in the
831 Santa Clara valley, California, from a large interferometric synthetic aperture radar
832 data set, *J. Geophys. Res.*, 108(B9), 2416, doi:10.1029/2002JB002267

833 Schuur, E. A. G., McGuire, A. D., Schädel, C., Grosse, G., Harden, J. W., Hayes, D. J.,
834 Hugelius, G., Koven, C. D., Kuhry, P., Lawrence, D. M., Natali, S. M., Olefeldt, D.,
835 Romanovsky, V. E., Schaefer, K., Turetsky, M. R., Treat, C. C. & Vonk, J. E. (2015).

836 Climate change and the permafrost carbon feedback, *Nature*, 520, 171–179,
837 doi:10.1038/nature14338.

838 Shiklomanov, N. I., Streletskiy, D. A., Little, J. D., & Nelson, F. E. (2013). Isotropic thaw
839 subsidence in undisturbed permafrost landscapes, *Geophys. Res. Lett.*, 40, 6356–6361,
840 doi:10.1002/2013GL058295.

841 Short, N., Brisco, B., Couture, N., Pollard, W., Murnaghan, K., Budkewitsch, P. (2011). A
842 comparison of TerraSAR-X, RADARSAT-2 and ALOS-PALSAR interferometry for
843 monitoring permafrost environments, case study from Herschel Island, Canada,
844 *Remote Sens. Environ.*, 115, 3491—3506, doi:10.1016/j.rse.2011.08.012

845 Siberian Times (2019). https://siberiantimes.com/other/others/news/hell-on-fire-raging-bush-
846 inferno-at-batagai-depression-giant-gash-in-the-tundra/

847 Strozzi, T., Antonova, S., Günter, F., Mätzler, E., Vieira, G., Wegmüller, U., Westermann, S.
848 & Bartsch, A. (2018). Sentinel-1 SAR Interferometry for Surface Deformation
849 Monitoring in Low-Land Permafrost Areas, *Remote Sens.*, 10, 1360,
850 doi:10.3390/rs10091360

851 Taber, S. (1929). Frost heaving, *J. Geol*., 37:428–461. doi:10.1086/623637

852 Taber, S. (1930). The mechanics of frost heaving, *J. Geol*., 38:303–317. doi:10.1086/623720

853 Wagner, A. M., Lindsey, N. J., Dou, S., Gelvin, A., Saari, S., Williams, C., Ekblaw, I., Ulrich,
854 C., Borglin, S., Morales, A., Ajo-Franklin, J. (2018). Permafrost Degradation and
855 Subsidence Observations during a Controlled Warming Experiment, *Sci. Rep*.,
856 8:10980, doi:10.1038/s41598-018-29292-y

857 Watanabe, K. & Mizoguchi, M. (2000). Ice configuration near a growing ice lens in a
858 freezing porous medium consisting of micro glass particles, *J. Cryst. Growth*, 213,
859 135–140.

860 Wettlaufer, J. S. & Worster, M.G (2006). Premelting Dynamics, *Annu. Rev. Fluid Mech.*,
861 38:427–52

862 Worster, M. G., & Wettlaufer, J. S. (1999). The fluid mechanics of premelted liquid films.
863 In Fluid Dynamics at Interfaces (ed. W. Shyy & R. Narayanan), pp. 339–351.
864 Cambridge University Press.

865 Yoshikawa, K., Bolton, W. R., Romanovsky, V. E., Fukuda, M., & Hinzman, L. D. (2002).
866 Impacts of wildfire on the permafrost in the boreal forests of Interior Alaska, *J.*
867 *Geophys. Res.,* 107(D1), 8148, doi:10.1029/2001JD000438.

868 Zhang, Y., Wolfe, S. A., Morse, P. D., & Fraser, I. O. R. H. (2015). Spatiotemporal impacts of
869 wildfire and climate warming on permafrost across a subarctic region, Canada, *J.*
870 *Geophys. Res. Earth Surf.*, 120,2338–2356, doi:10.1002/2015JF003679.

871 Zwieback, S., Hensley, S., & Hajnsek, I. (2015). Assessment of soil moisture effects on L-
872 band radar interferometry. *Remote Sens. Environ.,* 164, 77-89, doi:
873 10.1016/j.rse.2015.04.012

874 Zwieback, S., Liu, X., Antonova, S., Heim, B., Bartcsh, A., Boike, J., & Hajnsek, I. (2016).
875 A Statistical Test of Phase Closure to Detect Influences on DInSAR Deformation
876 Estimates Besides Displacements and Decorrelation Noise: Two Case Studies in
877 High-Latitude Regions. *IEEE Trans. Geosci. Remote Sens.,* 54(9), 5588-5601, doi:
878 10.1109/TGRS.2016.2569435.

879 **Table 1.** Data list of ALOS2 for interferograms in Figures 4a-4e and Figure 7.

Interferogram	Dates (YYYYMMDD)	Perpendicular Baseline (m)	Temporal Baseline (days)
Short-term images (Figure 4)			
(a)	20170617-20170729	11	48
(b)	20170729-20171009	-104	72
(c)	20171009-20171202	-46	54
(d)	20171202-20180310	283	98
(e)	20180310-20180602	-259	84
Long-term images (Figure 7)			
(a)	20151010-20161008	98	364
(b)	20160730-20170729	97	364
(c)	20161008-20171007	-104	364
(d)	20161217-20171202	-146	350
(e)	20170617-20180602	-118	350
(f)	20170729-20180728	-200	364
(g)	20180310-20190309	-191	364
(h)	20180602-20190601	41	364

880

881 **Table 2.** Data list of Sentinel-1 for Stacked images in Figures 4f-4j and interferograms in
882 Figure 6.

Stack	Interferogram	Dates (YYYYMMDD)	Perpendicular Baseline (m)	Temporal Baseline (day)
(f)	(1)	20170611-20170623	23	12
	(2)	20170623-20170705	-74	12
	(3)	20170705-20170729	-15	24
(g)	(4)	20170729-20170810	43	12
	(5)	20170810-20170822	-30	12
	(6)	20170822-20170903	36	12
	(7)	20170903-20170915	-15	12
	(8)	20170915-20170927	-54	12
	(9)	20170927-20171009	35	12
(h)	(10)	20171009-20171021	80	12
	(11)	20171021-20171102	32	12
	(12)	20171102-20171114	-46	12
	(13)	20171114-20171126	-89	12
	(14)	20171126-20171208	26	12
(i)	(15)	20171208-20171220	114	12
	(16)	20171220-20180101	43	12
	(17)	20180101-20180113	-66	12
	(18)	20180113-20180125	-143	12
	(19)	20180125-20180206	34	12
	(20)	20180206-20180218	59	12
	(21)	20180218-20180302	26	12
	(22)	20180302-20180314	-25	12
(j)	(23)	20180314-20180407	-91	24
	(24)	20180407-20180419	-43	12
	(25)	20180419-20180501	155	12
	(26)	20180501-20180513	-29	12
	(27)	20180513-20180525	-74	12
	(28)	20180525-20180606	-73	12

883